ZEUS-prel-06-010

Submitted to the
XXXIII International Conference on High Energy Physics
July 26 - August 2, 2006, Moscow, Russia

Abstract: **Session: QCD hard interactions / QCD soft interactions**

Leading neutron energy and p_T distributions in deep inelastic scattering and photoproduction at HERA

ZEUS Collaboration

Abstract

The production of energetic neutrons in *ep* collisions has been studied with the ZEUS detector at HERA. The neutron energy and p_T distributions were measured with a forward neutron calorimeter and tracker in a $40\,\mathrm{pb}^{-1}$ sample of inclusive deep inelastic scattering (DIS) and dijet photoproduction data, and a sub-sample of $6\,\mathrm{pb}^{-1}$ of inclusive photoproduction data. The photoproduction data are suppressed in the medium energy ranges, and has a steeper p_T^2 distribution than in deep inelastic scattering, consistent with the expectation from absorption. The distributions are compared to HERA measurements of leading protons. The neutron transverse-momentum distributions in DIS are compared to the predictions of models of pion exchange. The neutron energy distributions in photoproduction and DIS are compared to a model of pion exchange incorporating absorption.

1 Introduction

In ep scattering at HERA, a significant fraction of events contains a baryon carrying a large fraction of the incoming proton energy [1–3]. The production mechanism of these low-transverse-momentum leading baryons is not completely understood. Although leading neutrons can result from the fragmentation of the proton remnant, exchange models (Fig. 1) give a better description of the data. In this picture, the incoming proton emits a virtual particle which scatters on the photon emitted from the beam electron. The outgoing baryon, of energy E_B, carries a fraction $x_L = E_B/E_p$ of the beam energy, while the exchanged particle participates in the process with energy $(1 - x_L)E_p$.

In particular, one-pion exchange is a significant contributor to leading neutron production for large x_L [1]. For such a process the cross section for the semi-inclusive reaction $ep \rightarrow eXn$ factorizes into two terms:

$$\frac{d^2\sigma(W^2, Q^2, x_L, t)}{dx_L dt} = f_{\pi/p}(x_L, t)\sigma_{\gamma^*\pi}((1 - x_L)W^2, Q^2),$$

where Q^2 is the virtuality of the exchanged photon, W is the center-of-mass energy of the virtual photon-proton system and t is the square of the four-momentum of the exchanged pion. In terms of the measured quantities x_L and transverse momentum p_T, the pion virtuality is:

$$t \simeq -\frac{p_T^2}{x_L} - \frac{(1 - x_L)(m_n^2 - m_p^2 x_L)}{x_L}.$$

The flux of virtual pions emitted by the proton is represented by $f_{\pi/p}$ and $\sigma_{\gamma^*\pi}$ is the cross section of the virtual photon and virtual pion interaction with center-of-mass energy $\sqrt{1 - x_L}\,W$. If the cross section is assumed to be independent of t, the p_T distribution of produced neutrons is completely determined by the flux factor. Many parameterizations of the pion flux have been suggested in the literature [4–11]. They have the general form:

$$f_{\pi/p}(x_L, t) \propto \frac{-t}{(t - m_\pi^2)^2}(1 - x_L)^{\alpha(t)} F^2(x_L, t).$$

The power $\alpha(t)$ and the form factor $F(x_L, t)$ are model dependent with parameters extracted from low energy hadron-hadron scattering data.

One implication of exchange models is vertex factorization, which predicts that the dependence of the cross section on the baryon variables does not change for differing values of the variables at the lepton vertex. At the lepton vertex, the significant variable is Q^2. In a one-pion-exchange model, neutron absorption can occur through rescattering [12–15]. If the size of the n-π system is small compared to the size of the photon, the neutron can also scatter on the photon. The neutron can then migrate to lower x_L and higher p_T; the kinematic region it migrates to may be outside of the detector acceptance and it will not be detected. The rescattering can also transform the neutron into a charged baryon which may also escape detection. Since the size of the virtual photon is inversely related to Q^2, more neutron rescattering would be expected for photoproduction ($Q^2 \approx 0$) than for deep inelastic scattering (DIS, $Q^2 > \sim 1\,\mathrm{GeV}^2$).

Rescattering removes neutrons from small n-π systems. The size of the n-π system is inversely proportional to the neutron p_T, so rescattering removes neutrons with large p_T. Thus rescattering results in a depletion of neutrons at high p_T in photoproduction relative to DIS, a form of vertex factorization violation. Pion exchange models incorporate a variation of the mean size of the n-π system as a function of x_L. This results in an x_L dependence of the absorption, again a violation of vertex factorization. Previous studies with leading neutrons [2] show a mild violation of vertex factorization with the expected increase of rate when going from photoproduction to DIS. Similar effects have been seen for leading protons [3].

This paper presents measurements of the x_L and p_T distributions of leading neutrons. The neutrons are in samples of DIS and inclusive photoproduction events. Neutron production is also studied in dijet photoproduction events, where the large transverse energy E_T of the jets provides a hard scale analogous to the large Q^2 in DIS events. The x_L and p_T distributions in DIS and photoproduction are compared to test vertex factorization. The neutron measurements are compared to similar measurements of leading protons at HERA. The neutron p_T distributions in DIS are compared to several pion exchange models with various choices of their parameters.

The present data have recently been the focus of a detailed theoretical analysis with the aim of extracting information on the pion structure function as well as the rapidity gap suppression factor, relevant for diffractive processes in hadron-hadron collisions. [14, 15]. The reader is referred to these works for a description of the model and a detailed comparison with the present data.

2 Detectors

A detailed description of the ZEUS detector can be found elsewhere [16]. A brief outline of the components that are most relevant for this analysis is given below.

The high-resolution uranium–scintillator calorimeter (CAL) [17] consists of three parts: the forward (FCAL), the barrel (BCAL) and the rear (RCAL) calorimeters. Each part is subdivided transversely into towers and longitudinally into one electromagnetic section (EMC) and either one (in RCAL) or two (in BCAL and FCAL) hadronic sections (HAC). The smallest subdivision of the calorimeter is called a cell. The CAL energy resolutions, as measured under test-beam conditions, are $\sigma(E)/E = 0.18/\sqrt{E}$ for electrons and $\sigma(E)/E = 0.35/\sqrt{E}$ for hadrons (E in GeV). The EMC sections were used to detect scattered positrons in DIS events and the RCAL was used to trigger on the dissociated photon in photoproduction events.

Bremsstrahlung $ep \to e\gamma p$ and the photoproduction of hadrons $ep \to eX$ are tagged using the luminosity (LUMI) detectors [18]. The bremsstrahlung photons are measured with a lead-scintillator calorimeter located $Z = -107\,\mathrm{m}$[1] from the interaction point in the positron-beam direction. A similar calorimeter at $Z = -35\,\mathrm{m}$ from the interaction point is used to measure positrons scattered at very small angles in an energy range 5-20 GeV, with an energy resolution of $0.19\sqrt{E}$ (E in GeV).

The forward neutron calorimeter (FNC) [19–21] was installed in the HERA tunnel at $\theta = 0$ degrees and at $Z = 106\,\mathrm{m}$ from the interaction point in the proton-beam direction after the leading proton spectrometer, as depicted in Fig. 2. It was used for the 1995-2000 data taking. The FNC is a lead-scintillator calorimeter with an energy resolution for hadrons measured in a test beam to be $\sigma_E/E = 0.70/\sqrt{E(\,\mathrm{GeV})}$. Three planes of veto counters were located in front of the FNC.

In the spring of 1998 a forward neutron tracker (FNT) was installed in the FNC at a depth of one interaction length. It is a scintillator hodoscope designed to measure the position of neutron showers. Each scintillator finger is 16.8 cm long, 1.1 cm wide and 0.5 cm deep: 17 are used for X position reconstruction and 15 for Y. Figure 3 shows the position of the FNT hodoscope in the FNC relative to the incoming neutron beam. The irregular outlined area shows the geometric acceptance defined by magnet apertures. This limits detection to neutrons with production angles less than 0.75 mrad, allowing transverse momenta in the range $p_T \le E_n\theta_{\max} = 0.69x_L\,\mathrm{GeV}$. The allowed kinematic regions in p_T^2 and t are shown in Fig. 4. Scans by a ^{60}Co radioactive source were performed to calibrate and monitor both detectors. The position resolution of neutron showers in the FNT of $\pm 0.23\,\mathrm{cm}$ was measured by placing an adjustable collimator in front of the outermost veto counter of the FNC during special test and calibration runs.

3 Data selection and analysis

The data for this analysis were collected in 2000 when HERA collided 27.5 GeV positrons with 920 GeV protons. Separate triggers were used to collect DIS, dijet photoproduction, and inclusive photoproduction events with leading neutrons.

[1] The ZEUS coordinate system is a right-handed Cartesian system, with the Z axis pointing in the proton beam direction, referred to as the "forward direction", and the X axis pointing left towards the center of HERA. The coordinate origin is at the nominal interaction point.

The DIS events were collected using a trigger that detected the scattered electron in the CAL. In the offline analysis, the scattered electron was required to be at least 3 cm from the inner edge of the beam-pipe hole in the RCAL. This limited the acceptance to the kinematic range $Q^2 > 2\,\mathrm{GeV}^2$ with a mean photon virtuality of $\langle Q^2 \rangle \simeq 14\,\mathrm{GeV}^2$. The quantity $E - P_Z = \sum_i E_i(1-\cos\theta_i)$, with the sum running over all calorimeter cells, was required to be in the range $35 < E - P_Z < 65\,\mathrm{GeV}$; the lower cut reduced photoproduction background with a misidentified electron. The integrated luminosity of the DIS sample was $40\,\mathrm{pb}^{-1}$.

Dijet photoproduction events were collected with a trigger requiring at least two jets, selected by the cone algorithm, with tranverse energies $E_T^{jet} > 4.5\,\mathrm{GeV}$, and pseudorapidities of $|\eta^{jet}| < 2.5$ in the lab frame. In the offline analysis the k_T algorithm was used to reconstruct the jets. Jets were required to be in the pseudorapidity range $-1.5 < \eta^{jet} < 2.5$; at least one such jet was required to have $E_T^{jet} > 7.5\,\mathrm{GeV}$ and one jet to have $E_T^{jet} > 6.5\,\mathrm{GeV}$. The reconstructed γp center-of-mass energy W was required to be in the range $130 < W < 280\,\mathrm{GeV}$. Events with a scattered electron detected in the CAL were rejected; this restricted the range of Q^2 to less than $\sim 1\,\mathrm{GeV}^2$. The integrated luminosity of the dijet photoproduction sample was $40\,\mathrm{pb}^{-1}$.

The inclusive photoproduction events were collected during the last part of the 2000 running period using a trigger that required at least 5 GeV in the positron tagger in coincidence with at least 464 MeV in the RCAL EMC [22]. The acceptance of the positron tagger limited the photon virtuality to $Q^2 < 0.02\,\mathrm{GeV}^2$, with a median Q^2 of approximately $\langle Q^2 \rangle \simeq 5 \times 10^{-5}\,\mathrm{GeV}^2$. Offline, events were required to have less than 1 GeV in the photon tagger to reject overlapping bremsstrahlung events. The integrated luminosity of the photoproduction sample was $6\,\mathrm{pb}^{-1}$.

The DIS and inclusive photoproduction triggers required at least 165 GeV of energy to be deposited in the FNC. Offline cuts were used to select clean neutron candidates, and further cuts were applied to select neutrons with a well reconstructed position.

Figure 5 shows a scatter plot of reconstructed hits in the FNT from a sample of DIS events. The irregular curve is the aperture expected from a Monte Carlo simulation of the beam line. The simulation also models significant amounts of dead material in some regions of the aperture. There is good agreement between the simulation and the data distribution. For example, the deficit of events observed around $Y \sim 10.5\,\mathrm{cm}$ is well reproduced by the simulation of dead material. The energy resolution of the FNC, the position resolution of the FNT, and the inherent p_T-spread in the HERA proton beam are also simulated. The latter corresponds to a smearing of the zero-degree point by 0.45 cm horizontally and 1.0 cm vertically, significantly larger than the FNT resolution. The simulation was tuned to match the neutron x_L and p_T distributions separately for the DIS, dijet photoproduction, and inclusive photoproduction samples.

Reconstruction of the neutron scattering angle θ_n requires knowledge of the zero-degree point. By passing a symmetric distribution of neutrons through the simulation and fitting to the data, this point was determined to an accuracy of ±0.2 cm in X and Y. This uncertainty is included in the systematic uncertainties on the p_T^2 distributions. Other significant contributions to the uncertainties are the FNC energy scale uncertainty of $\pm2\%$ and the uncertainties in the dead material map.

The three data samples studied here have widely varying inclusive cross sections σ_{inc}, i.e. the cross section without a leading neutron requirement. In order to compare neutron production in the different processes it is useful to normalize the cross section with a leading neutron, σ_{LN}, by the inclusive cross section:

$$r = \frac{\sigma_{\mathrm{LN}}}{\sigma_{\mathrm{inc}}}.$$

Differences in this relative neutron yield r indicate differences in the neutron production mechanism for the different processes. The acceptance for detecting the different types of events in the central ZEUS detector is independent of the neutron requirement; this cancels in the yield r, eliminating systematic uncertainties from this acceptance. Therefore only the acceptance of the forward neutron detectors is needed for measuring the relative yield.

4 Neutron x_L and p_T^2 distributions in DIS

The corrected p_T^2 distributions in DIS for different x_L bins are shown in Fig. 6. They are presented as normalized doubly differential distributions $(1/\sigma_{\mathrm{DIS}})d^2\sigma_{\mathrm{LN}}/dx_L dp_T^2$, where σ_{DIS} is the cross section of DIS events without a neutron requirement. The aperture limitation $\theta_n < 0.75\,\mathrm{mrad}$ is seen in the varying p_T^2 ranges plotted. The line on each plot is a fit to the functional form $d\sigma_{\mathrm{LN}}/dp_T^2 \propto \exp(-bp_T^2)$, which gives a good description of the data. The dependence of the intercepts $(1/\sigma_{\mathrm{DIS}})d^2\sigma_{\mathrm{LN}}/dx_L dp_T^2|_{p_{T^2=0}}$ and the slopes b on x_L are shown in Figs. 7 and 8. The intercepts fall to zero at the endpoint $x_L = 1$, are roughly constant in the region $x_L = 0.4 - 0.8$, and rise steeply as x_L approaches zero. Below $x_L = 0.3$ the slopes are consistent with zero; they rise linearly in the range $0.3 < x_L < 0.85$ to a value of $b \simeq 8\,\mathrm{GeV}^{-2}$, and then decrease slightly at higher x_L. The systematic uncertainties from the effects discussed in Section 3, which are highly correlated, are shown by the shaded band in Figs. 7 and 8.

Figure 9 shows the normalized differential distribution $(1/\sigma_{\mathrm{DIS}})d\sigma_{\mathrm{LN}}/dx_L$ for neutrons in DIS with scattering angles $\theta_n < 0.75\,\mathrm{mrad}$, corresponding to the kinematic range $p_T^2 < 0.476x_L^2\,\mathrm{GeV}^2$. It falls to zero at the endpoint $x_L = 1$, reaches a maximum near

$x_L = 0.7$, and falls as x_L decreases due to the vanishing region of p_T space. The systematic uncertainties, which are highly correlated, are shown by the shaded band in Fig. 9.

5 Comparison of neutron distributions in DIS and photoproduction

To minimize effects of energy calibration and beam position drifts, only the subset of DIS data collected simultaneously with the inclusive photoproduction data are used for comparisons between the two sets. The ratio of the normalized differential distributions:

$$\rho(x_L) = \frac{\frac{1}{\sigma(\gamma p \to X)} \frac{d\sigma(\gamma p \to nX)}{dx_L}}{\frac{1}{\sigma(\gamma^* p \to X)} \frac{d\sigma(\gamma^* p \to nX)}{dx_L}},$$

for the scattering angle cut $\theta_n < 0.75\,\mathrm{mrad}$ is shown in Fig. 10. In the range $0.2 < x_L < 0.55$, the ratio drops slightly but rises for higher x_L values, exceeding unity for $x_L > 0.9$. The curves in Fig. 10 are discussed in Section 7.

The p_T^2 distributions for both samples, normalized to unity at $p_T^2 = 0$, are shown in Fig. 11. The photoproduction distributions are clearly steeper in the range $0.6 < x_L < 0.9$, with relatively fewer neutrons at high p_T^2. The difference of the slopes $\Delta b = b(Q^2 < 0.02\,\mathrm{GeV}^2) - b(Q^2 > 2\,\mathrm{GeV}^2)$ is less sensitive to systematic effects than each of the individual slopes. These values are plotted in Fig. 12. The slopes for photoproduction are clearly larger in the range $0.6 < x_L < 0.9$, with $\Delta b = 0.5$–$1.0\ \mathrm{GeV}^{-2}$. The depletion of neutrons at large p_T^2 is qualitatively consistent with the expectations from absorption models.

The normalized differential distributions $(1/\sigma_{\mathrm{inc.}})d\sigma_{\mathrm{LN}}/dx_L$ for neutrons with $\theta_n < 0.75\,\mathrm{mrad}$ are shown for DIS and dijet photoproduction in Fig. 13. There are significantly fewer neutrons in dijet photoproduction than in DIS for $x_L > 0.6$. The slopes of the p_T^2 distributions are compared in Fig. 14. The values for the dijet photoproduction data are similar in values to those for DIS, but increase more steeply with x_L. The limited statistics of the dijet photoproduction data do not provide a significant measure of differences from the DIS slopes.

6 Comparison to leading protons

ZEUS has also reported x_L distributions for leading protons in the region $p_T^2 < 0.04\,\mathrm{GeV}^2$ [23]. The neutron x_L distributions were also measured in the same region, using the FNT measurement of p_T. The results are compared in Fig. 15. There are approximately twice as many protons in the range $0.6 < x_L < 0.9$ of the proton measurement. If only isospin 1 particle exchanges contribute to proton production, there should be half as many protons as neutrons. Thus, in a particle exchange model, exchanges of different isospin must be invoked to account for the observed rate of proton production.

The slopes of the p_T^2 distributions for leading protons and neutrons are shown in Fig. 16. The proton slopes do not have the same steep x_L dependence as the neutron slopes. The two samples have similar values of b near $x_L \approx 0.8$, the region where pion exchange is expected to dominate for both processes.

7 Comparison to models

The slopes can be compared to parameterizations of the pion flux $f_{\pi/p}$. Although $f_{\pi/p}$ is not an exponential in p_T^2, at fixed x_L the models can be fit to the form $\exp(-bp_T^2)$ and the resulting $b(x_L)$ values compared to the data. All of the parameterizations in the literature give values for the slopes larger than the data [4–11]. Most of them also have the wrong x_L dependence of the slopes. The models with the best agreement are shown in Fig. 17. The simplest model, with the form factor $F(x_L, t) = 1$, is closest in magnitude to the data [4]. Other models with more detailed parameterizations show the turnover of the slopes near $x_L \approx 0.85$ [7, 8].

The dashed curve in Fig. 10 is the expectation for the suppression of leading neutrons in photoproduction relative to DIS from a model of absorption [13]. Although the data lie above the curve, they qualitatively follow the trend of the curve. γp interaction cross sections have a power law dependence $\sigma \propto W^{2\lambda}$, with different values of λ for DIS and photoproduction. Assuming that $\gamma\pi$ interactions have the same dependence, and recalling that $W_{\gamma\pi} = \sqrt{1 - x_L} W_{\gamma p}$, this results in a dependence of the ratio of photoproduction and DIS cross sections proportional to $(1 - x_L)^{\Delta\lambda}$, with $\Delta\lambda \approx -0.1$. Applying this to the absorption suppression factor results in the solid curve in Fig. 10. The data is well described by the absorption model with the correction for different W dependences.

8 Conclusions

The x_L and p_T distributions of leading neutrons in photoproduction and DIS events at HERA have been measured. The p_T^2 distributions are well described by an exponential $\exp(-bp_T^2)$. The slope b rises linearly with x_L in the range $0.3 < x_L < 0.85$ for both photoproduction and DIS.

There are relatively fewer neutrons in inclusive photoproduction than in DIS for $x_L < 0.9$, with the depletion growing as x_L decreases to $x_L \approx 0.5$. The depletion is consistent with a model of pion exchange incorporating absorption of the neutrons. The b values for photoproduction lie above the DIS values in the range $0.6 < x_L < 0.9$, which is qualitatively consistent with the expectations from absorption models. In dijet photoproduction there are relatively fewer neutrons than in DIS for $x_L > 0.4$. Within the statistical precision of the data the slopes b are nearly the same in dijet photoproduction and DIS.

In the kinematic region $0.6 < x_L < 0.9$ and $p_T^2 < 0.04\,\text{GeV}^2$ there are approximately twice as many leading protons as neutrons. This indicates that leading proton production proceeds through exchanges in addition to pure isovector (e.g. pion) exchange. Unlike for neutrons, the slopes b for leading protons are roughly constant an a function of x_L, agreeing with the neutron slopes near $x_L \approx 0.8$ where pion exchange is expected to dominate both processes.

The measured $b(x_L)$ dependence in DIS has been compared with various pion exchange models. All models give values larger than seen in the data. The simplest model is closest in magnitude to the data; other models reproduce the measured shape of $b(x_L)$.

References

[1] ZEUS Coll., M. Derrick et al., Phys. Lett. **B 384**, 388 (1995);
H1 Coll., C. Adloff et al., Eur. Phys. J. **C 6**, 587 (1999);
ZEUS Coll., J. Breitweg et al., Nucl. Phys. **B 596**, 3 (2001).

[2] ZEUS Coll., J. Breitweg et al., Nucl. Phys. **B 637**, 3 (2002).

[3] H1 Coll., C. Adloff et al., Nucl. Phys. **B 619**, 3 (2001);
ZEUS Coll., J. Breitweg et al., Nucl. Phys. **B 658**, 3 (2003).

[4] M. Bishari, Phys. Lett. **B 38**, 510 (1972).

[5] B. Kopeliovich, B. Povh and I. Potashnikova, Z. Phys. **C 73**, 125 (1996).

[6] N.N. Nikolaev et al., Phys. Rev. **D 60**, 014004 (1999).

[7] L.L. Frankfurt, L. Mankiewicz and M.I. Strikman, Z. Phys. **A 334**, 343 (1989).

[8] K. Golec-Biernat, J. Kwiecinski and A. Szczurek, Phys. Rev. **D 56**, 3955 (1997).

[9] M. Przybycien, A. Szczurek and G. Ingelman, Z. Phys. **C 74**, 509 (1997).

[10] A. Szczurek, N.N. Nikolaev and J. Speth, Phys. Lett. **B 427**, 383 (1998).

[11] W. Melnitchouk, J. Speth and A.W. Thomas, Phys. Rev. **D 59**, 014033 (1998).

[12] N.N. Nikolaev, J. Speth and B.G. Zakharov, Preprint KFA-IKP(TH)-1997-17 (hep-ph/9708290), KFA-IKP, 1997.

[13] U. D'Alesio and H.J. Pirner, Eur. Phys. J. **A 7**, 109 (2000).

[14] A.B. Kaidalov, V.A. Khoze, A.D. Martin and M.G. Ryskin, Preprint IPPP-06-10, DCPT-06-20 (hep-ph/0602215), 2006.

[15] V.A. Khoze, A.D. Martin and M.G. Ryskin, Preprint IPPP-06-36, DCPT-06-72 (hep-ph/0606213), 2006.

[16] ZEUS Coll., U. Holm (ed.), *The ZEUS Detector.* Status Report (unpublished), DESY (1993), available on `http://www-zeus.desy.de/bluebook/bluebook.html`.

[17] M. Derrick et al., Nucl. Inst. Meth. **A 309**, 77 (1991);
A. Andresen et al., Nucl. Inst. Meth. **A 309**, 101 (1991);
A. Caldwell et al., Nucl. Inst. Meth. **A 321**, 356 (1992);
A. Bernstein et al., Nucl. Inst. Meth. **A 336**, 23 (1993).

[18] J. Andruszków et al., Preprint DESY-92-066, DESY, 1992;
ZEUS Coll., M. Derrick et al., Z. Phys. **C 63**, 391 (1994);
J. Andruszków et al., Acta Phys. Pol. **B 32**, 2025 (2001).

[19] S. Bhadra et al., Nucl. Inst. Meth. **A 354**, 479 (1995).

[20] ZEUS Coll., FNC group, S. Bhadra et al., Nucl. Inst. Meth. **A 394**, 121 (1997).

[21] ZEUS FNC Group, S. Bhadra et al., *Proc. of the Seventh International Conference on calorimetry in High Energy Physics, Tuscon, Arizona, November 1997*, E. Cheu et al. (ed.), p. 295. World Scientific, Singapore (1998).

[22] ZEUS Coll., S. Chekanov et al., Nucl. Phys. **B 627**, 3 (2002).

[23] ZEUS Coll., S. Chekanov et al., Nucl. Phys. **B 658**, 3 (2003).

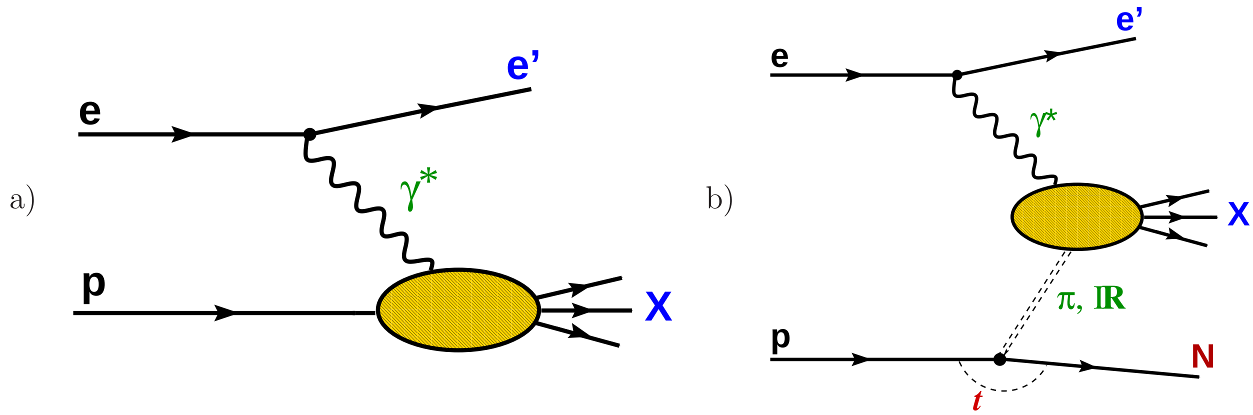

Figure 1: *a) HERA ep scattering event with the final-state baryon in the proton-fragmentation system, X. b) Leading baryon production via an exchange process.*

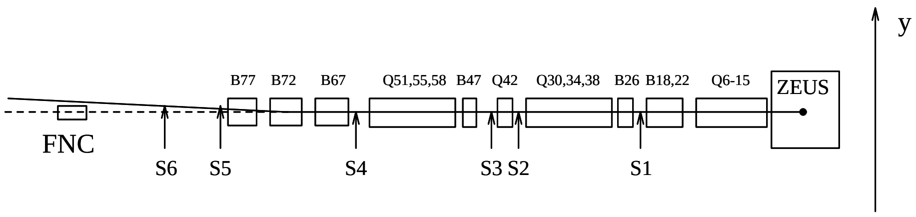

Figure 2: *The proton beamline downstream from the ZEUS interaction region. The proton beam is bent upward by approximately 6 mrad by the dipole magnets B67–B77 near Z=+70 m. The FNC is located on the zero-degree line at Z=+105.5 m. S1–S6 show the locations of the ZEUS leading proton spectrometer.*

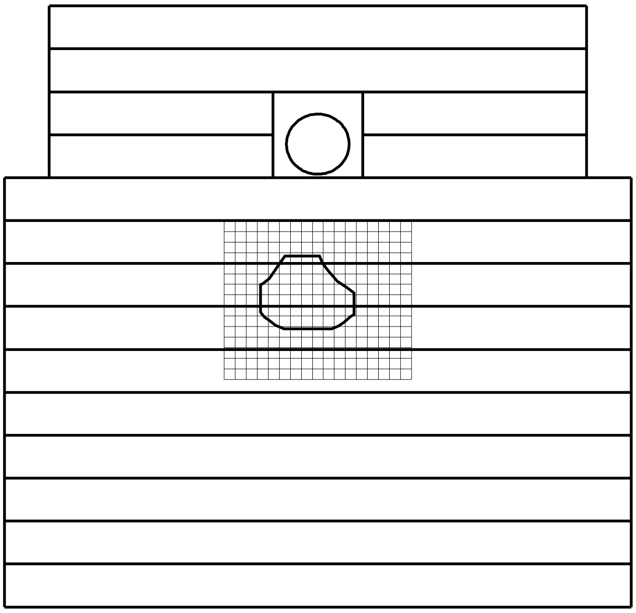

Figure 3: *Diagram of the FNC/FNT assembly. The heavy lines show the 5 cm vertical segmentation of the front part of the FNC. The hole through the third and fourth towers from the top allows the proton beam to pass through the calorimeter. The 17×15 grid of small squares shows the fingers of the FNT hodoscopes. The irregular curve shows the geometric aperture defined by upstream beamline elements, and the darkened square shows the zero-degree point.*

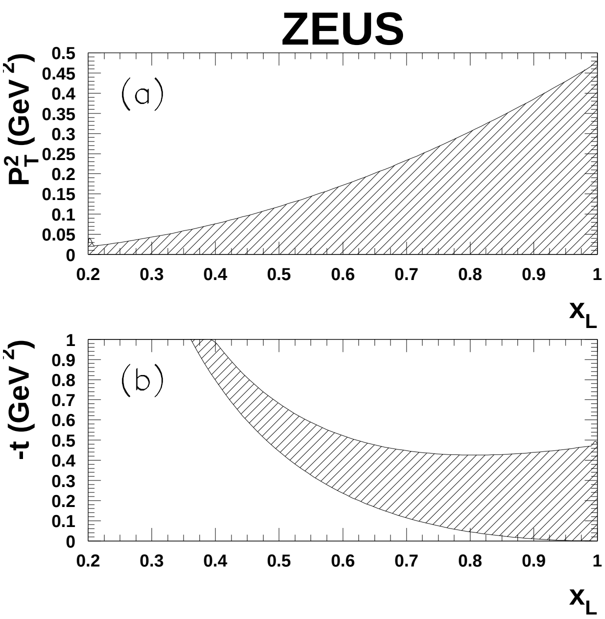

Figure 4: *The kinematic regions in (a) p_T^2 and (b) t covered by the angular acceptance of the FNC ($\theta_n < 0.75\,mrad$) are shown as shaded bands.*

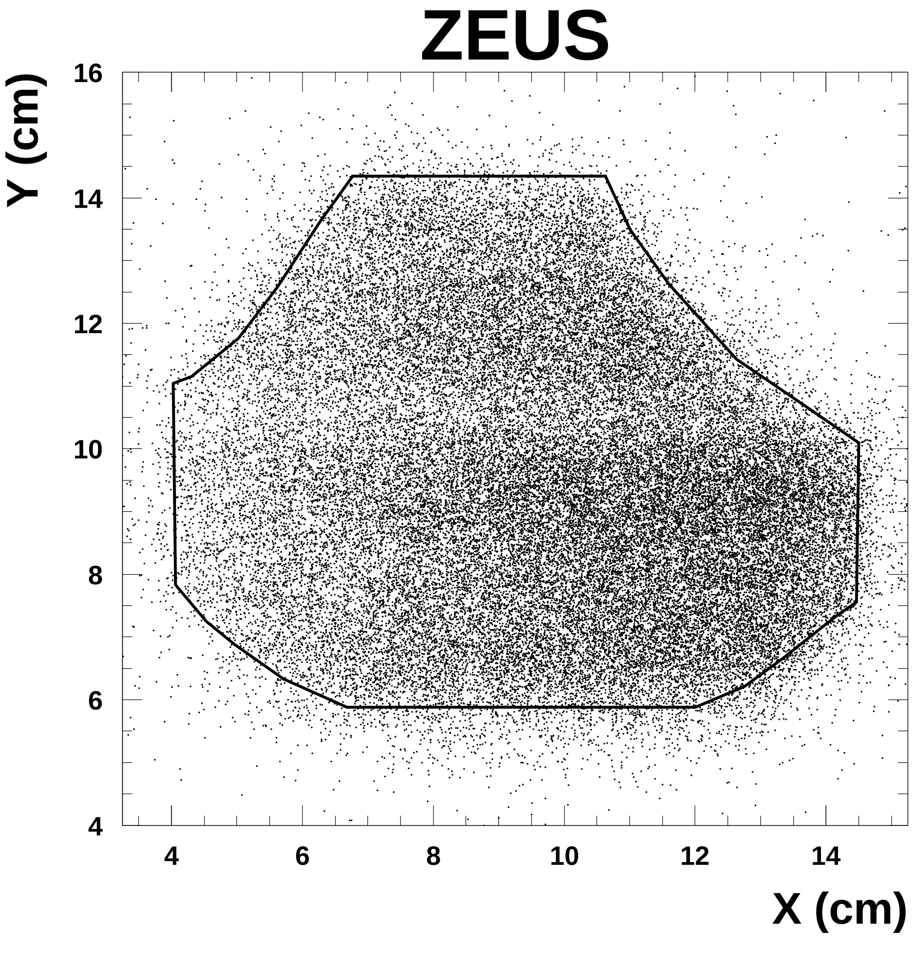

Figure 5: *Scatter plot of hits in the FNT. The irregular curve is the geometric aperture defined by upstream beamline elements as modeled in the Monte Carlo. The zero-degree point is at* $X = 12.5$ *cm,* $Y = 8.3$ *cm.*

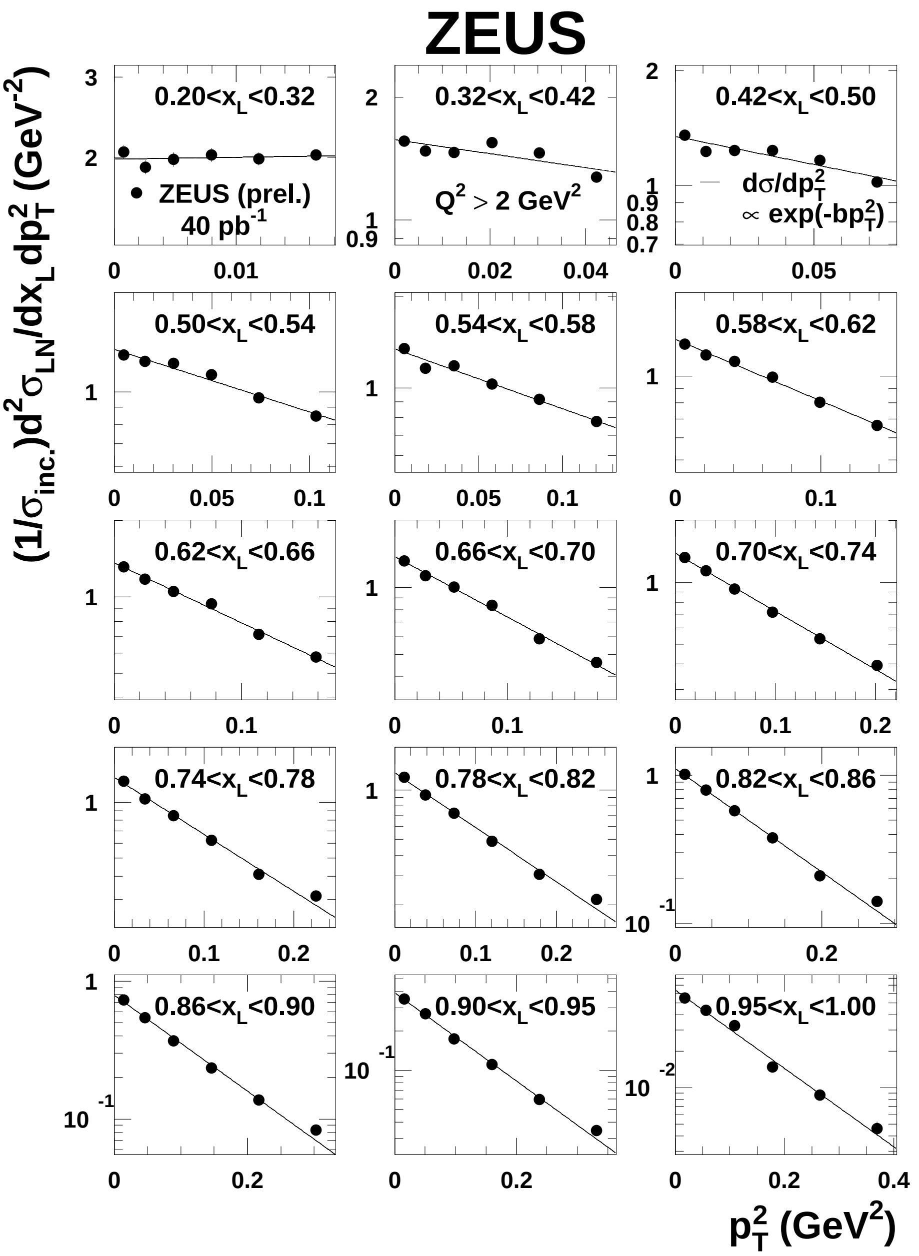

Figure 6: *The p_T^2 distributions for DIS. Note the logarithmic vertical scale and the varying p_T^2 ranges. The statistical errors are shown by a vertical error bar; in most cases they are smaller than the plotted symbol. The line on each plot is the result of a fit to the form $d\sigma_{\rm LN}/dp_T^2 \propto \exp(-bp_T^2)$.*

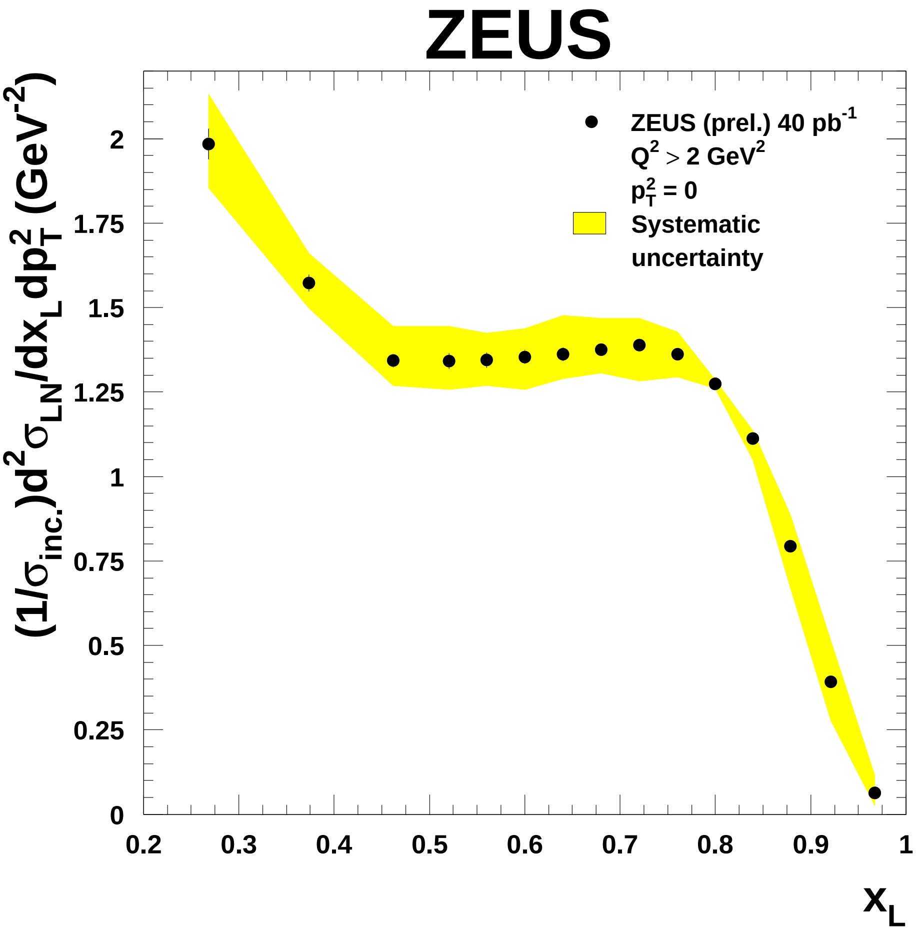

Figure 7: *The intercepts* $(1/\sigma_{\rm DIS})d^2\sigma_{\rm LN}/dx_L dp_T^2|_{p_T^2=0}$ *versus* x_L *from fits of the* p_T^2 *distributions in DIS to the form* $d\sigma_{\rm LN}/dp_T^2 \propto \exp(-bp_T^2)$ *over the* p_T^2 *ranges shown in Fig. 6. The error bars show the statistical uncertainties; the shaded band shows the systematic uncertainties.*

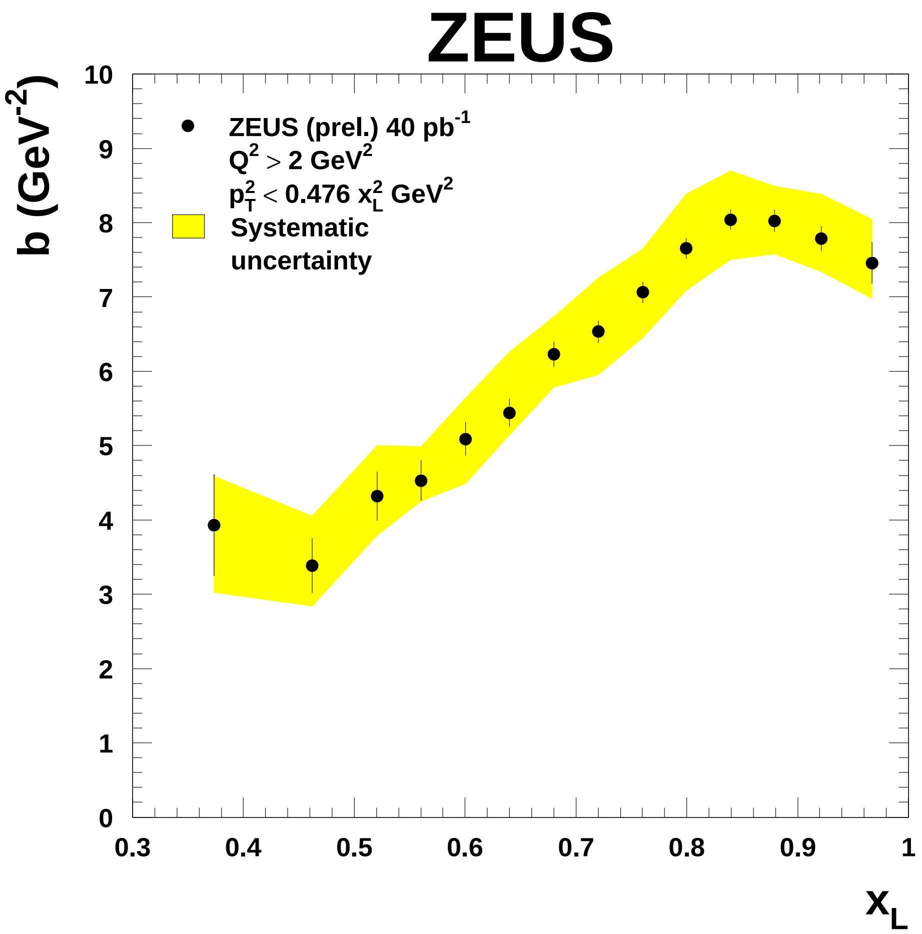

Figure 8: *The slopes* b *versus* x_L *from fits of the* p_T^2 *distributions in DIS to the form* $d\sigma_{\rm LN}/dp_T^2 \propto \exp(-bp_T^2)$ *over the* p_T^2 *ranges shown in Fig. 6. The error bars show the statistical uncertainties; the shaded band shows the systematic uncertainties.*

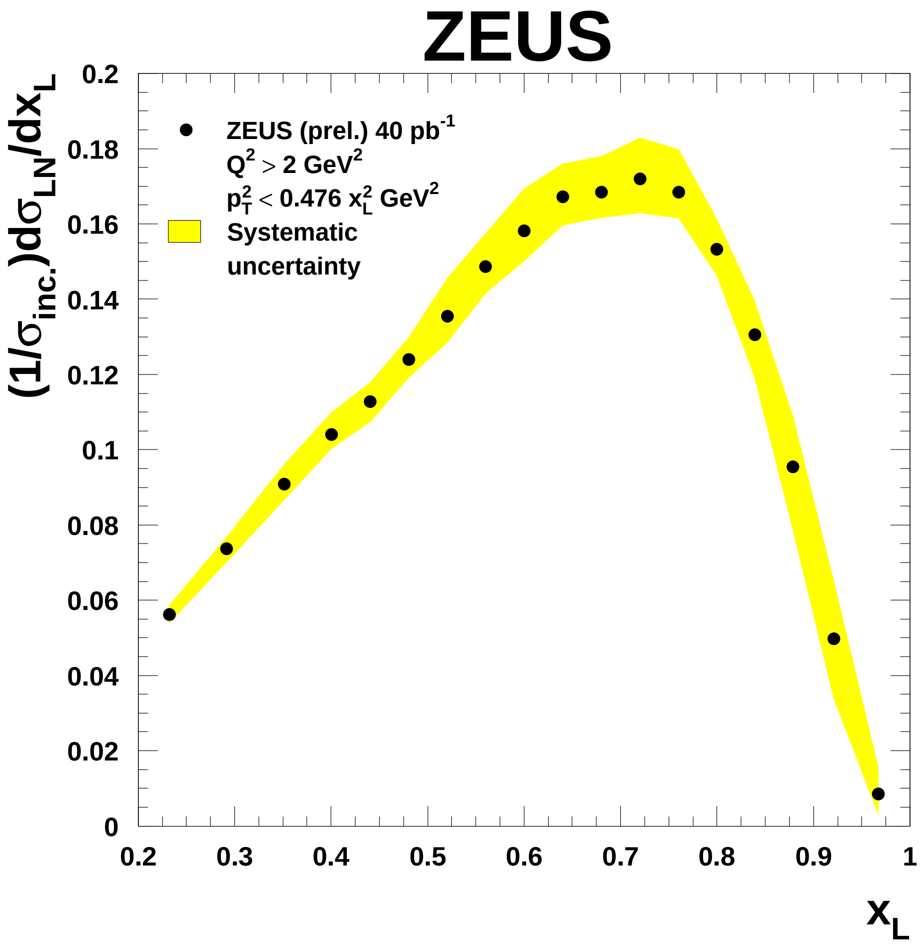

Figure 9: *The distribution $(1/\sigma_{\rm DIS})d\sigma_{\rm LN}/dx_L$ for neutrons in DIS with scattering angles $\theta_n < 0.75\,mrad$, corresponding to the kinematic range $p_T^2 < 0.476x_L^2\ GeV^2$. The error bars show the statistical uncertainties; the shaded band shows the systematic uncertainties.*

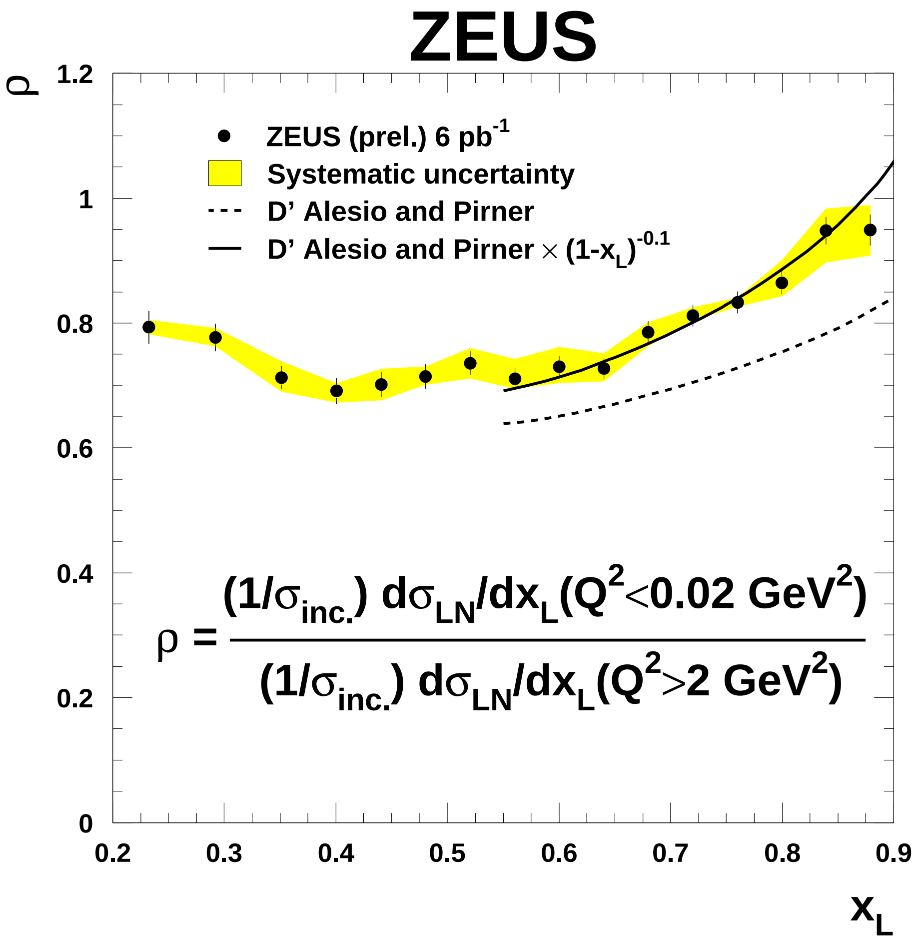

Figure 10: *The ratio of the x_L distributions inclusive photoproduction over DIS, normalized as described in the text, for neutrons with scattering angles $\theta_n < 0.75\,mrad$, corresponding to the kinematic range $p_T^2 < 0.476 x_L^2\ GeV^2$. The error bars show the statistical uncertainties; the shaded band shows the systematic uncertainties. The curve is prediction of a rescattering model*

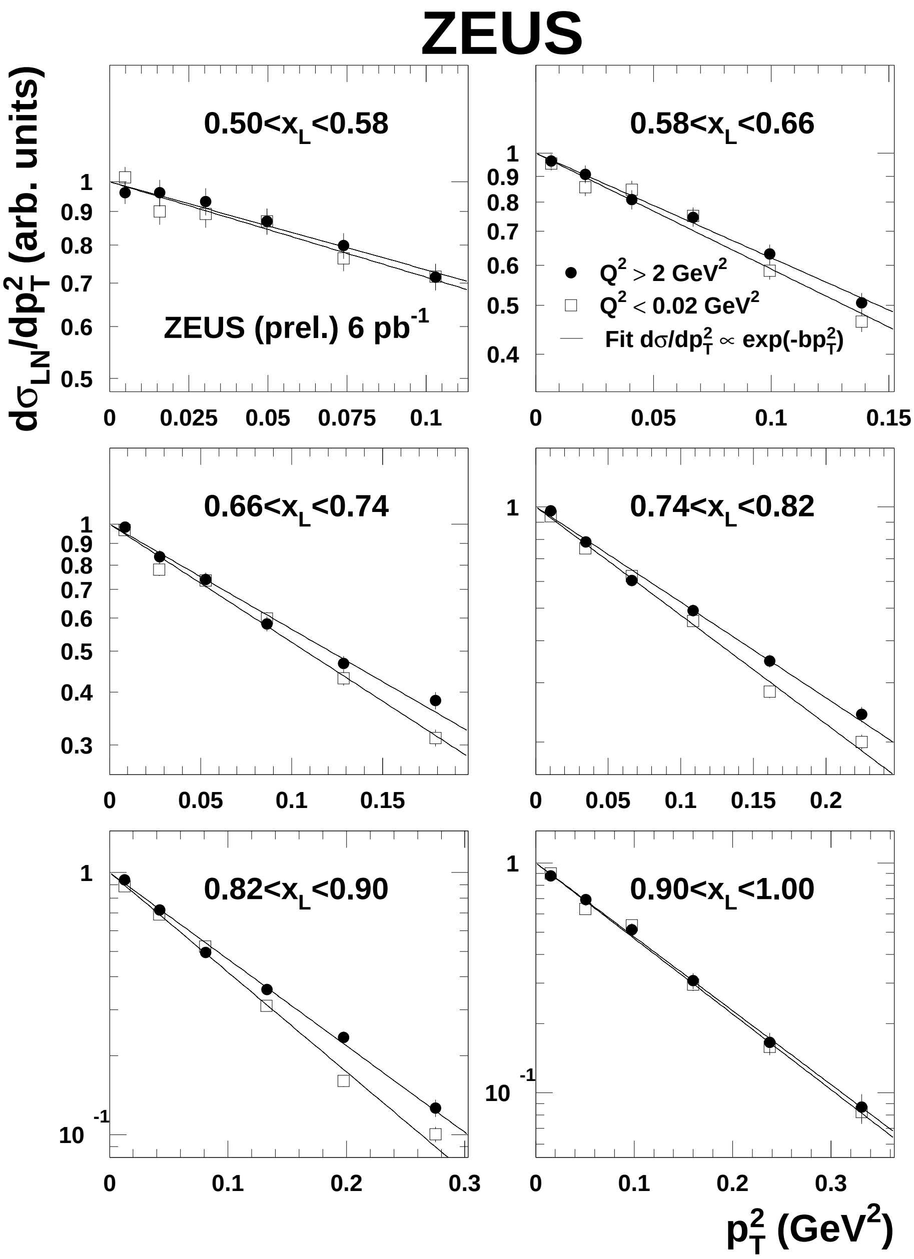

Figure 11: *The p_T^2 distributions for photoproduction and DIS. They are each normalized to unity at $p_T^2 = 0$. Note the logarithmic vertical scale and the varying p_T^2 ranges. The statistical errors are shown by a vertical error bar; in some cases they are smaller than the plotted symbol. The lines on each plot are the results of fits to the form $d\sigma_{\mathrm{LN}}/dp_T^2 \propto \exp(-bp_T^2)$.*

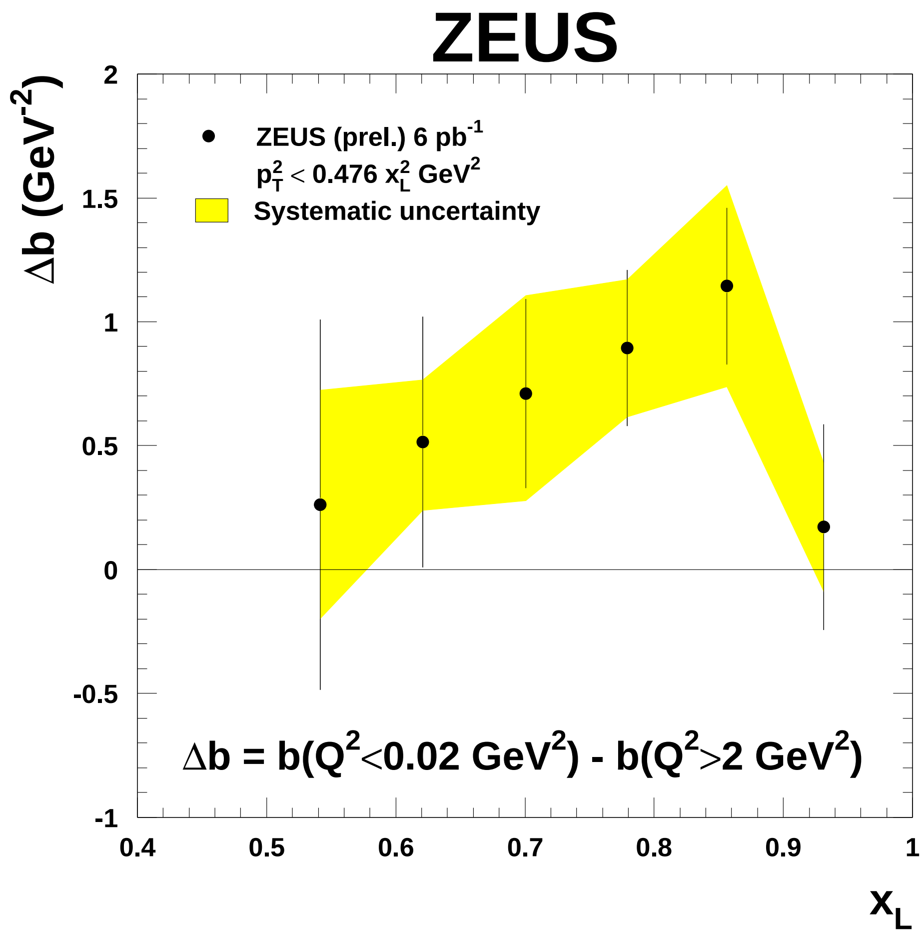

Figure 12: *The differences between slopes in photoproduction and DIS Δb versus x_L. The error bars show the statistical uncertainties; the shaded band shows the systematic uncertainties.*

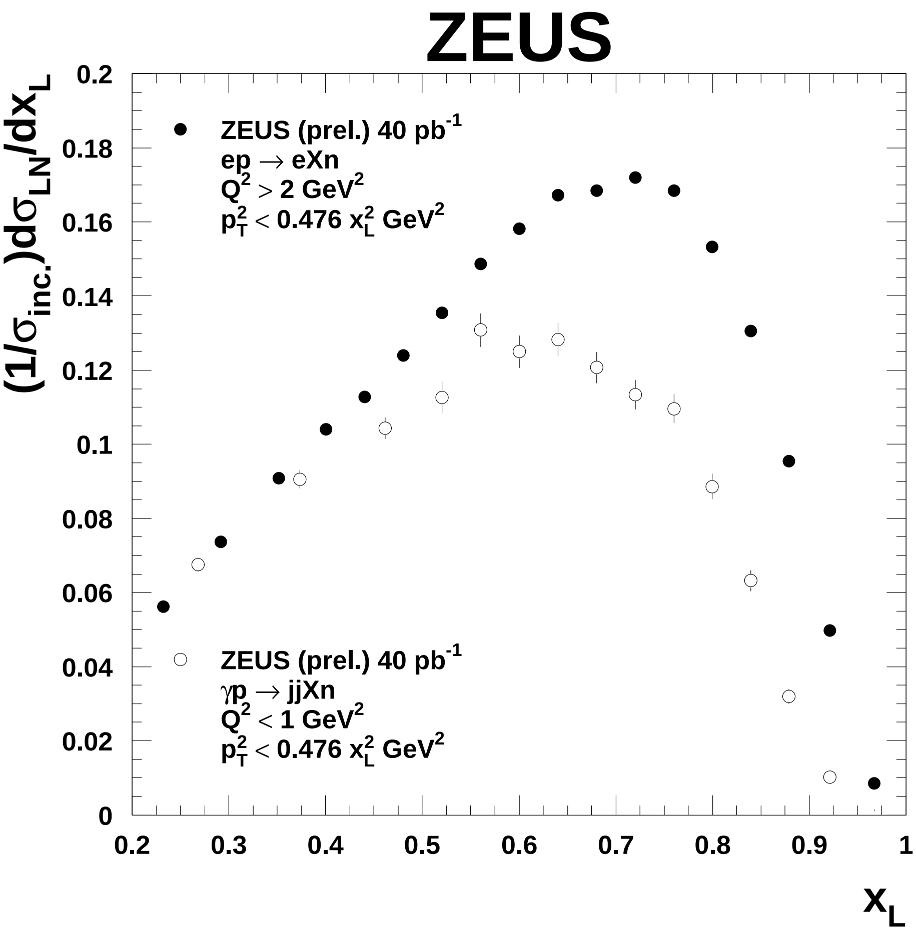

Figure 13: *The normalized differential distributions $(1/\sigma_{\rm inc.})d\sigma_{\rm LN}/dx_L$ for neutrons with $\theta_n < 0.75$ mrad for DIS and dijet photoproduction.*

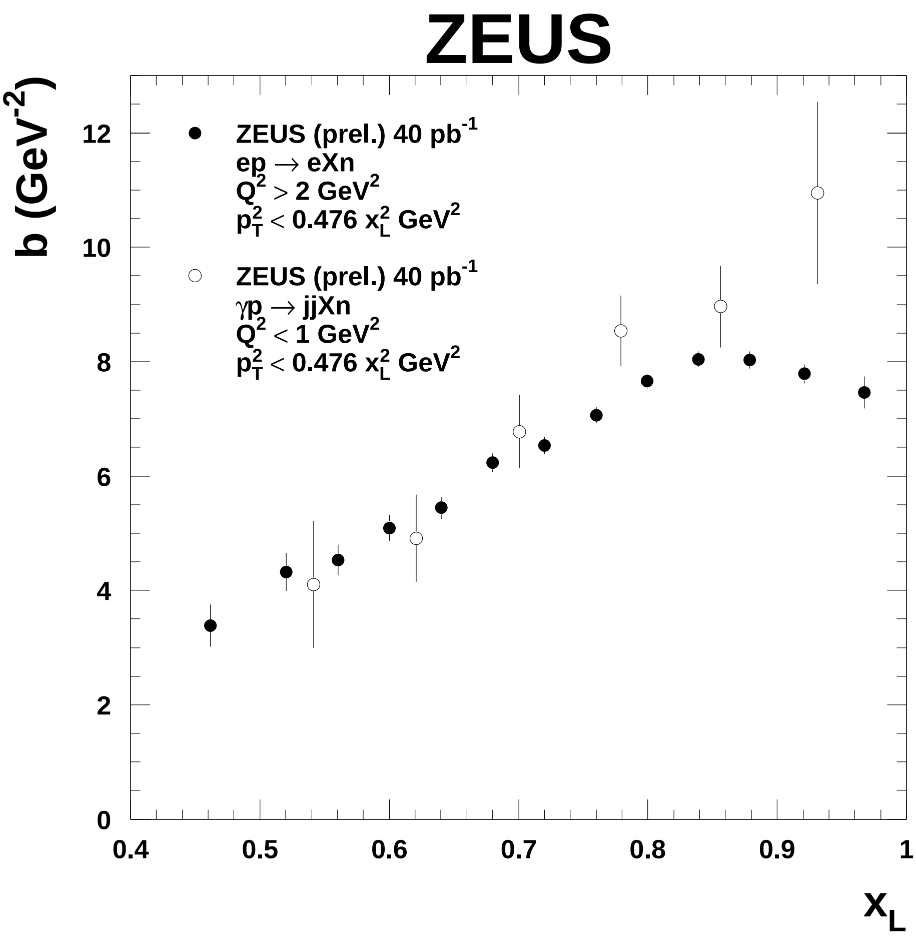

Figure 14: *The slopes of the p_T^2 distributions for DIS and dijet photoproduction.*

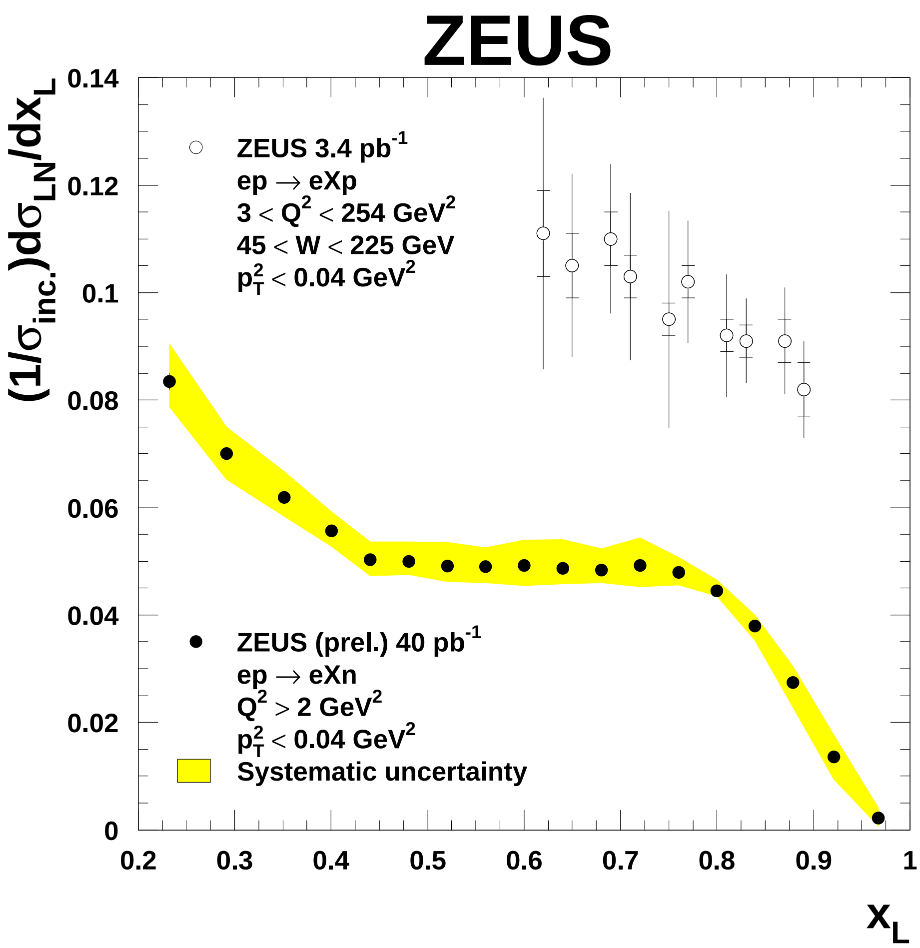

Figure 15: *The normalized differential distributions $(1/\sigma_{\rm DIS})d\sigma_{\rm LN}/dx_L$ for leading protons and neutrons in the range $p_T^2 < 0.04\ GeV^2$. For the leading neutron points the error bars show the statistical uncertainties; the shaded band shows the systematic uncertainties. For the leading proton points the inner error bars show the statistical uncertainty only; the full error bars show the statistical and systematic uncertainties added in quadrature.*

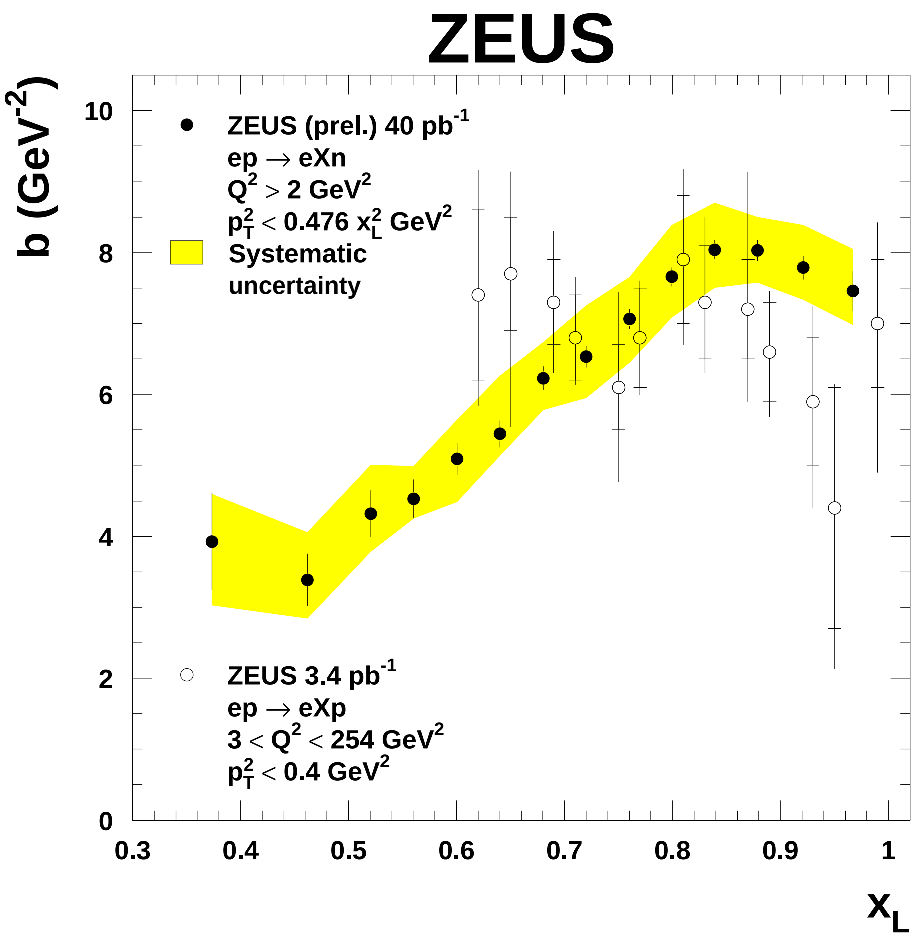

Figure 16: *The slopes of the p_T^2 distributions for leading neutrons and protons in DIS. For the leading neutron points the error bars show the statistical uncertainties; the shaded band shows the systematic uncertainties. For the leading proton points the inner error bars show the statistical uncertainty only; the full error bars show the statistical and systematic uncertainties added in quadrature.*

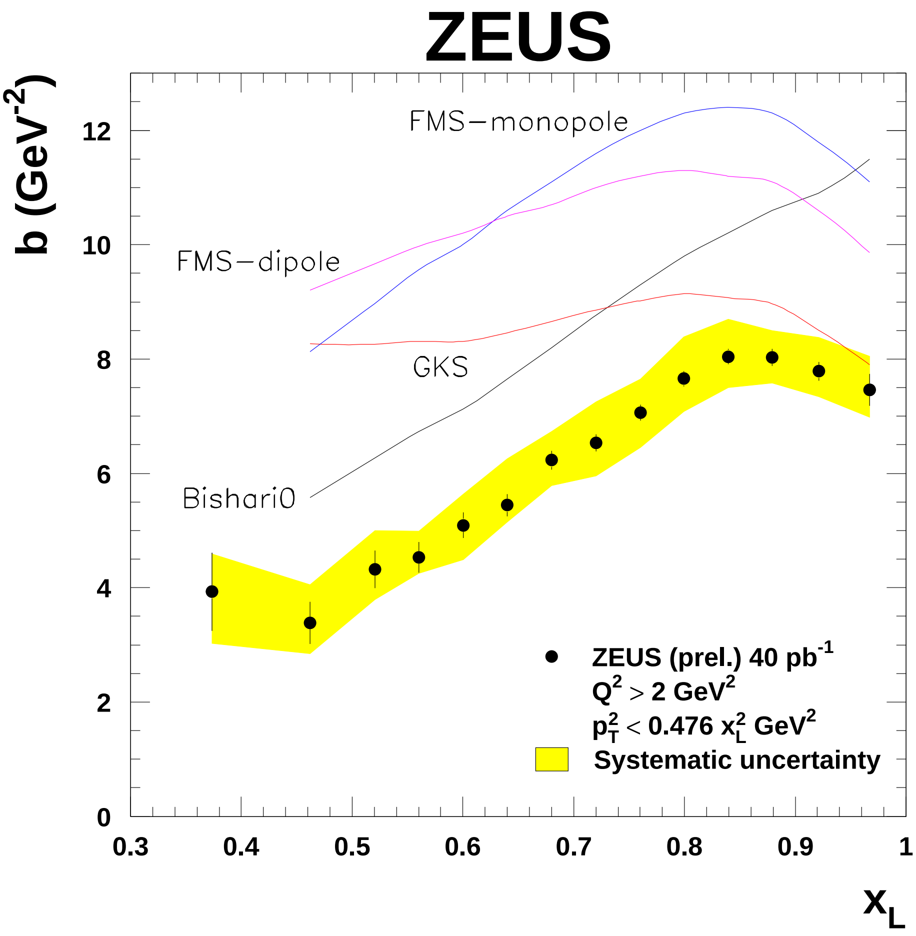

Figure 17: *The measured slopes b compared to the predictions of models of one-pion exchange alone. The error bars show the statistical uncertainties; the shaded band shows the systematic uncertainties. The curves are labeled by the authors' name or initials cited in the text.*